Energy Landscapes of Supramolecular Peptide–Drug Conjugates Directed by Linker Selection and Drug Topology

Matthew J. Sis,[†] Zhou Ye,[†] Katherine La Costa,[†] Matthew J. Webber[†, *]

†- University of Notre Dame, Department of Chemical & Biomolecular Engineering, Notre Dame, IN 46556 USA
*- mwebber@nd.edu

ABSTRACT: Peptide–drug conjugates that self-assemble into supramolecular nanomaterials have promise for uses in drug delivery. These discrete molecular species offer high and precise drug loading, affording efficient carriers for various therapeutic agents. Their peptide modules, meanwhile, enable biological targeting and stimuli-responsive function while also ordering the assembled nanostructure. The often hydrophobic drug payload likewise acts as a directive for self-assembly in aqueous media. Though accessible synthetic methods have allowed for extensive exploration of the peptide design space, the specific contributions of the drug molecule and its linker to the resulting assembly have been less explored. Hydrophobic drugs frequently have planar domains, conjugated π-systems, and isolated polar groups, which in turn can lead to specific and directional self-interactions. These energies of interaction affect the free energy landscape of self-assembly, and may impact the form and assembly process of the desired nanomaterial. Here, two model supramolecular peptide–drug conjugates (sPDCs) are explored, composed of the corticosteroid dexamethasone conjugated to a conserved peptide sequence *via* two different linker chemistries. The choice of linker, which alters the orientation, rotational freedom, and number of stereoisomers of the prodrug in the final sPDC, impacts the mechanism and energetic barrier of assembly as well as the nano/macro scale properties of the resultant supramolecular materials. Accordingly, this work demonstrates the non-zero energetic contributions of the drug and its linker to sPDC self-assembly, provides a quantitative exploration of the sPDC free energy landscape, and suggests design principles for the enhanced control of sPDC nanomaterials to inform future applications as therapeutic drug carriers.

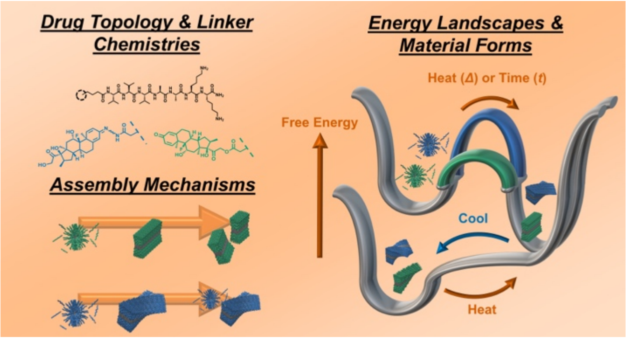

KEYWORDS: Biomaterials; Drug Delivery; Supramolecular Chemistry; Pharmaceutics; Stimuli-Responsive Materials

1. INTRODUCTION

The field of drug delivery remains in need carrier-based technologies that can more efficiently encapsulate and effectively target therapeutics.[1] The creation of materials *via* supramolecular association provides one useful design approach that may be more fully exploited in the context of drug delivery.[2] In particular, the supramolecular assembly of oligopeptides offers multiple routes to realize drug carriers through either passive encapsulation or labile conjugation of a therapeutic; the peptide building blocks also afford facile integration of biological targeting units.[3–5] Simple and robust synthetic schemes facilitate creation of peptide-based systems with molecular-level control over the nanoscale form and properties of a material.[6,7] Supramolecular interactions in these materials are dynamic and both the covalent and non-covalent interactions comprising these materials may have engineered sensitivity to chemical environment and respond to disease-relevant stimuli.[8–10] Covalently linked drugs have been incorporated into the designs of a variety of supramolecular peptide–drug conjugates (sPDCs).[11,12] An attractive outcome is the realization of so-called "one-component nanomedicine" offering a discrete and defined molecular entity that constitutes both the therapeutic and carrier, offering tunable and quantitative drug loading.[13–15] Commonly, the drugs used in these designs are hydrophobic, offering a directive cue driving self-assembly in aqueous environments; a diverse array of therapeutics have been incorporated including chemotherapeutics, H_2S donors, anti-inflammatories, and multi-drug combinations.[9,16–19] The assembled forms are furthermore useful as localized hydrogel depots and systemically circulating nanocarriers.[20,21]

It is increasingly appreciated that features such as molecular design, environmental conditions, and the rate and/or order of applied stimuli dictate the formation of both equilibrium and non-equilibrium states in supramolecular materials.[22–24] Accordingly, an underexplored facet of sPDCs is the complex free energy landscape and assembly pathways traversed to realize the final supramolecular materials; such considerations are likely to have implications on the functional use of these materials. Specifically, contributions of the drug moiety itself along with its mode of conjugation must be better explored to understand its role in dictating the thermodynamics of the final assembly. Hydrophobic drugs commonly have planar domains, regions of π-bond conjugation, and isolated polar groups, which together strongly favor ordered and directional drug–drug interactions in the desolvated core of an assembly. Molecular dynamics studies on sPDC assemblies prepared with a hydrophobic and highly π-conjugated chemotherapeutic, camptothecin, have found the drug to adopt a preferred orientational stack and twist in the final nanofiber assembly; the formation of durable drug–drug interactions was also found to occur prior to inter-peptide β-sheet hydrogen bonding in the evolution of these assemblies.[25–27] Thus, supramolecular interactions of the drug payload can impact the thermodynamics of the final system, and in some cases even hinder or completely disrupt intended associations of the fused peptide domain. As an example, a recent report required the iterative design of seventeen sPDCs before stable micelles with the desired properties were attained, with chemical modification of a drug domain hydroxyl group proving critical to serum stability of the nanomaterials.[28]

In light of these observations, a case study of how prodrug supramolecular chemistry impacts the thermodynamics of self-assembly and material outcomes in sPDC systems could prove instructive. Here, model sPDCs were prepared bearing the steroidal anti-inflammatory dexamethasone (DEX) conjugated by either a hydrazone or ester prodrug linker to a conserved amphiphilic peptide sequence. The molecular design arising from choice of conjugation chemistry impacted the geometric orientation, rotational freedom, and stereoisomerism of the drug. This seemingly minor alteration resulted in marked differences in both the mechanism and thermodynamics of self-assembly, and dictated disparate material properties of the resulting nanofibrillar hydrogels. These findings inform considerations for both the drug and linker in future rational design and development of sPDCs for applications as "one-component" drug carriers.

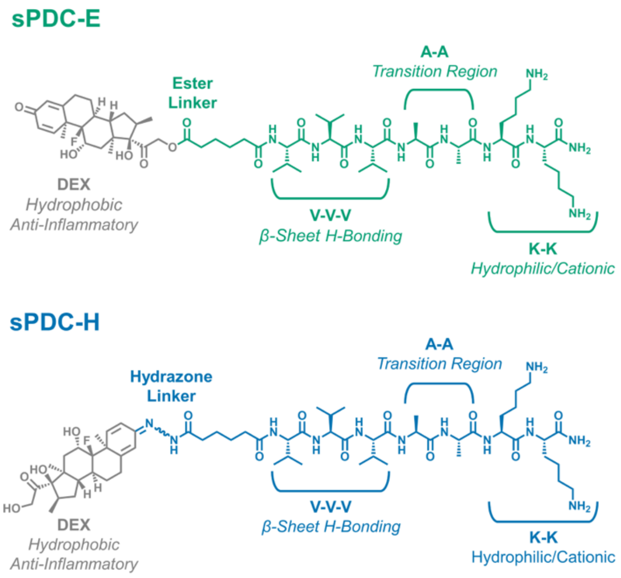

Figure 1: sPDC molecular design and rationale. Structures of sPDC-E (*top*) and sPDC-H (*bottom*). sPDCs incorporate prodrug-DEX, varying the identity of the linker used (ester or hydrazone) and concomitant drug topology. The peptide sequence, VVVAAKK, is conserved in both molecules.

2. RESULTS & DISCUSSION

2.1 Molecular Design of sPDCs. Towards the development of an injectable hydrogel leveraging sPDCs for the delivery of DEX, we coupled classic principles of peptide supramolecular assembly with common prodrug linker chemistries. DEX was anticipated as a good candidate for sPDC design due to its strongly hydrophobic nature (water solubility 0.089 mg/mL)[29] and its demonstrated ability to self-assemble when synthesized into amphiphilic small molecular prodrugs.[30,31] Accordingly, DEX was conjugated to a preserved peptide sequence using either an ester (sPDC-E) or hydrazone (sPDC-H) linker. The peptide sequence $V_3A_2K_2$ was adopted from work on peptide amphiphiles (PAs),[32] a class of materials that have similar design principles as sPDCs but typically employ a non-drug hydrophobic block. Aliphatic amino acids have the strongest thermodynamic favorability to participate in $\boldsymbol{\beta}$-sheets,[33] and valine (V) has been found to occur most commonly in β-sheet secondary structures of natural proteins.[34] Sequences of 2 to 3 valines are frequently used to stabilize PA nanofibers through interpeptide parallel β-sheets propagating along the fibrillar z-axis.[35,36] The subsequent amino acid blocks of alanine (A) and lysine (K) were chosen to provide flexibility to the peptide head and solubilize the molecule, respectively. Accordingly, it was rationalized that the combination of a hydrophobic DEX block coupled to an amphiphilic peptide domain will yield an sPDC design capable of self-assembling into one-dimensional nanostructures driven by a combination

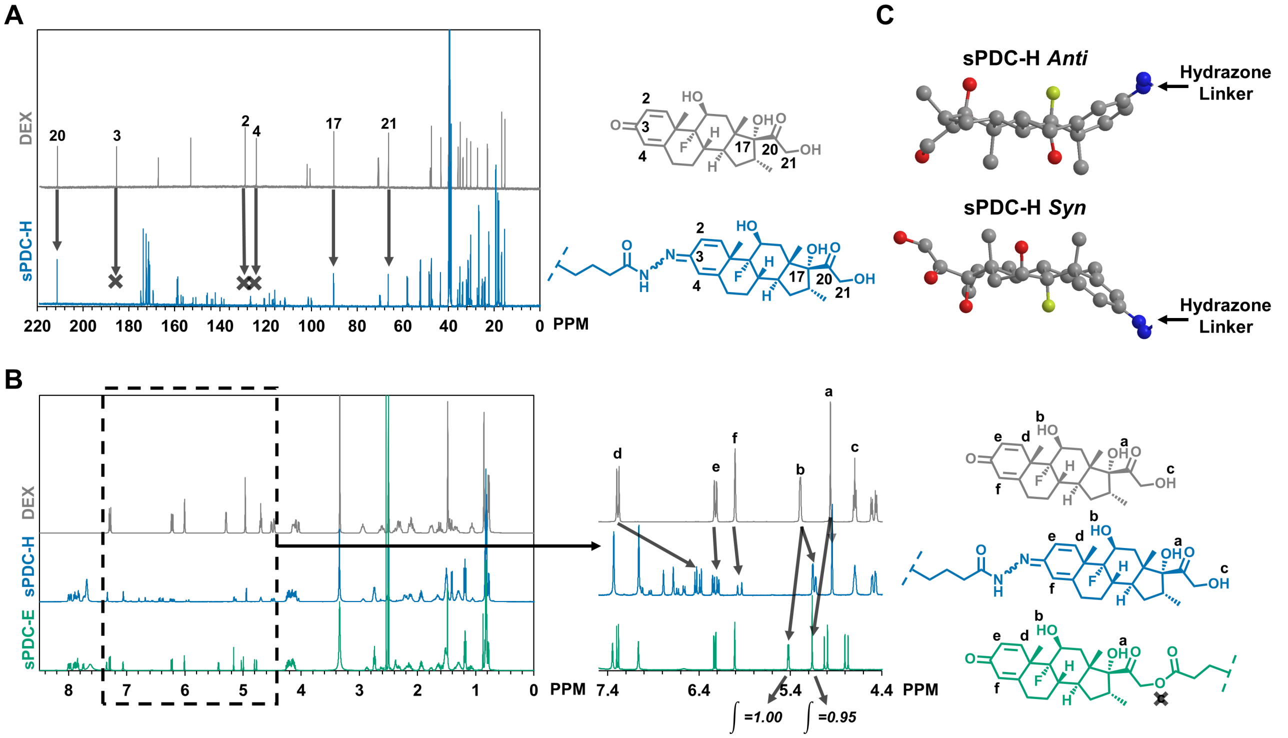

Figure 2: NMR analysis of sPDCs. (A) ^{13}C NMR of free DEX versus sPDC-H. Carbons 2-4 shifted completely from their original spectral positions, while carbons 17, 20, and 21 retain their original chemical shift. (**B**) ^{1}H NMR of free DEX versus sPDC-H and sPDC-E. In sPDC-H, signal shifts and splitting in protons 'a' and 'b-f' indicate syn/anti stereoisomerism of hydrazone-linked DEX. In sPDC-E, elimination of proton 'c' and 1:1 integration of protons 'a' and 'b' indicate only the primary hydroxyl reacts to form ester-linked DEX. (**C**) Molecular graphic of syn/anti stereoisomers in sPDC-H.

of hydrophobic drug association and interpeptide β-sheet formation. The molecular structures of these sPDCs and the intended functions of their various domains are outlined in ***Fig. 1.***

Esters and hydrazones are commonly used prodrug linker chemistries that are known to have differential rates of hydrolysis.[37,38] As such, these linkers were initially selected to explore the impacts of hydrolytic stability on the material properties of resulting sPDC nanofibrillar hydrogels. Indeed, release studies performed with the aid of analytical HPLC on hydrogels incubated in a bulk buffer demonstrated key differences in release properties. Importantly, the principal released species from hydrogels of both materials was the intact sPDC compound; sPDC-E released more total mass, with more prolonged release kinetics, than did sPDC-H. The latter instead was characterized by rapid mass loss in the initial days of incubation followed by a plateau in release. It is not possible to deconvolve the release of free molecular species from that arising by erosion of small-scale aggregates from the gel network, though vial inversion at the endpoint of the study verified that a gel remains intact in both samples. Importantly, at physiological pH sPDC-E showed some rupture of the ester pro-DEX bond, corresponding to release of ~10% of the gel payload as free drug. The hydrazone pro-DEX of sPDC-H, meanwhile, remained fully intact with no detectable free drug release. These findings follow expectations for the relative lability of each prodrug bond at physiological pH (***Fig. S5***). Also cognizant of the potential impacts of prodrug chemistry, linker directed topology, and possible isomerism on supramolecular assembly in this system, these two linkers also afforded an opportunity to carefully elucidate the impact of prodrug molecular designon sPDC assembly and nanofibrillar hydrogel formation. Accordingly, we carefully characterized the molecular structures of the sPDCs.

Specifically considering the design of sPDC-H, some disagreement is evident in the literature regarding the relative reactivity of the C3 versus C20 carbonyls of glucocorticoids when forming hydrazone prodrugs; reports have claimed exclusive conjugation at C3,[39,40] C20,[38,41] as well as a mixture of mono-conjugated constitutional isomers.[42–46] Studies using ^{13}C and ^{1}H NMR revealed that sPDC-H incorporates DEX exclusively through C3 conjugation. In the ^{13}C spectrum, signals for the C3 carbonyl and adjacent carbons C2 and C4 were completely shifted from their original positions in the spectrum of unmodified DEX, whereas carbons C17, C20, and C21 maintained their original chemical shifts following conjugation (***Fig. 2A***). This finding indicated the electronic environment of C3 is exclusively modified.

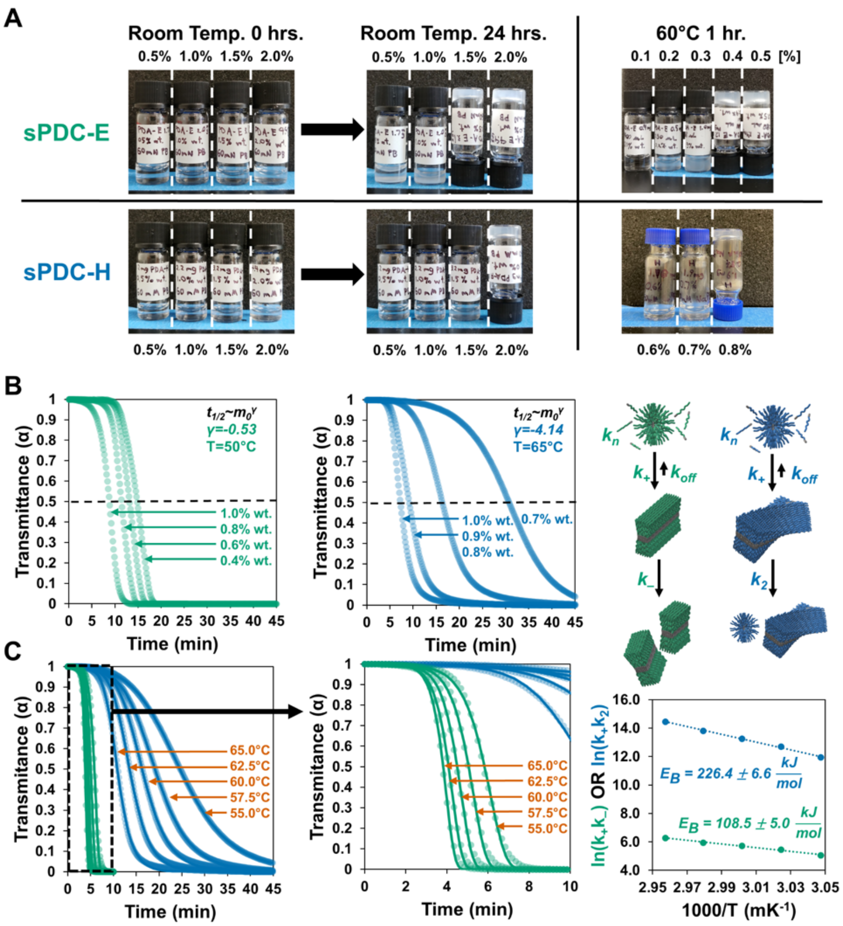

Figure 3: Mechanistic insights into "Slow" versus "Fast" hydrogelation. (**A**) Hydrogels of sPDC-E and sPDC-H are achievable by a "slow" path (days at room temp) or a "fast" path (1 h at 60°C). In both paths, gels of sPDC-E are attainable at lower minimum concentrations relative to sPDC-H. (**B**) Examination of the concentration dependent rates of hydrogelation reveals the self-assembly mechanisms of the sPDCs. Fitting of the half-times of concentration-dependent gelation studies reveals sPDC-E assembles through a nucleation, elongation, fragmentation (*NEF*) model, while sPDC-H assembles by nucleation, elongation, and secondary nucleation (*NE2°*). These dissimilar reaction mechanisms and corresponding kinetic steps are represented in the cartoon to the right. (**C**) Fitting the reaction models to isothermal gelation curves allows for the extraction and Arrhenius analysis of the combined rates for the propagation processes of assembly (sPDC-E = k_+k_-, sPDC-H = k_+k_2). By this analysis, the energy barrier towards assembly is roughly two times larger for sPDC-H versus sPDC-E.

Importantly, in the aforementioned literature exploring hydrazone-conjugated DEX, ^{13}C NMR has rarely been performed; these data thus enhance understanding for the likely site of hydrazone modification on DEX. The ^{1}H NMR spectrum further revealed both *syn-* and *anti-* diastereomers of the hydrazone conjugate, evidenced by the signal splitting at hydroxyl protons '*a*' and '*b*' as well as ring protons '*d-f*' (***Fig. 2B***). For clarity, proton '*d-f*' assignments were validated with gradient selected COSY NMR (***Fig. S6)***. Lastly, no evidence for di-peptide conjugated DEX was observed in ESI-MS or analytical-HPLC (***Figs. S7,S8***), again supporting conjugation exclusively at the C3 carbon. Thus, the product of the sPDC-H synthesis is a mixture of *syn-* and *anti-* C3 conjugates. Integration of protons *'d,' 'e,'* and *'f'* shows the isomers are racemic (***Fig. S9***). Taking the plane of the DEX corticoid ring system as reference, the stereoisomers can be thought to orient with the hydrazone linker either above or below this plane (***Fig. 2C***).

Analysis of sPDC-E focused primarily on verifying exclusive reactivity of DEX at its primary hydroxyl, which was clearly demonstrated in the ^{1}H NMR. The original chemical shift of primary hydroxyl proton '*c*' was completely eliminated from the spectrum, and secondary/tertiary hydroxyl peaks '*b*' and '*a*' integrated with a ratio of 1:1 relative to each other, as well as 1:1:3:1 relative to reference protons '*g*' and '*d*' on the peptide and DEX domains, respectively (***Fig. 2B, Fig. S9***). No evidence for di- or tri-peptide conjugation was seen by ESI-MS or analytical-HPLC on the final product (***Fig. S7,S8***), further supporting only one reactive site in the synthesis of sPDC-E. The formation of an ester linkage at this site furthermore does not result in stereoisomerization of sPDC-E.

2.2 Hydrogelation Kinetics: Divergent Assembly Mechanisms & Energy Barriers. In accordance with the rationale for molecular design, both sPDC-E and sPDC-H formed hydrogels in 60 mM phosphate buffer at pH 7.4 (***Fig. 3A***). Gross inspection performed at room temperature through vial inversion revealed formation of self-supporting hydrogels over 24 h, with apparent minimum gel concentrations of 1.5% wt. and 2.0% wt. for sPDC-E, and sPDC-H, respectively. Suspecting thermal energy may accelerate the assembly processes underlying gelation, samples were heated to 60°C for 1 h. The known impact of annealing peptide-based gelators, resulting in enhanced mechanical properties of nanofibers and hydrogels,[47,48] motivated this step. Interestingly, whereas most materials form hydrogels during the cooling stage of an annealing process, in these sPDCs gels emerged and appeared to be stabilized during the heating stage and persisted when cooled back to room temperature. Heating and cooling also resulted in a lower apparent minimum gel concentration of 0.4% wt. for sPDC-E and 0.7% wt. for sPDC-H. The relative minimum gel concentrations for these two sPDCs approximately matched the ratio of their critical aggregation concentrations, as determined by nile red dye sequestration assay to be 1.2 μM for sPDC-E and 2.4 μM for sPDC-H (***Fig. S10***). Taken together, these results suggest that while both sPDC-E and sPDC-H attain the desired material form of a hydrogel, there are possible differences in the mechanistic and thermodynamic routes underlying their assembly necessary to reach this outcome.

During the initial hydrogelation surveys, obvious visual differences were apparent in the rates of hydrogel formation for sPDC-E and sPDC-H. This finding suggested that further quantitative study of these rates may yield mechanistic and thermodynamic insight into the underlying supramolecular assembly. In the past decade, extensive work has led to material balance models of multi-step supramolecular polymerization.[49,50] Originally developed to study protein aggregation, these methods have also been applied to supramolecular fibrillar assemblies and hydrogelators.[51,52] According to published protocol and the free, web based *Amylofit* software, concentration and temperature dependent gelation/aggregation kinetics were analyzed to establish mechanisms of assembly and calculate contributions to the energy barriers (E_B) to assembly for sPDC-E and sPDC-H (***Fig. 3B,C***).[53]

Analyzing concentration-dependent kinetic curves affords insight into the mechanism of assembly and the corresponding material balance models appropriate for the sPDC-E and sPDC-H systems (***Fig. 3B***). In particular, all models under consideration by *Amylofit* predict a scaling relationship in concentration-dependent data, such that:

$$\boldsymbol{t_{1/2} \sim m_0^{\gamma}} \qquad (1)$$

where $\boldsymbol{t_{1/2}}$ is the half-time of reaction, $\boldsymbol{m_0}$ is the total mass in the system, and $\boldsymbol{\gamma}$ is a scaling exponent reflecting the concentration dependence of the dominant processes in the supramolecular reaction. Fitting **eqn. 1** to the half-time data (***Fig. S11***) yielded $\boldsymbol{\gamma}$=-0.53 and $\boldsymbol{\gamma}$=-4.14 for sPDC-E and sPDC-H, respectively. This analysis points to different supramolecular assembly mechanisms for the two systems, with sPDC-E corresponding to a *nucleation-elongation-fragmentation* (*NEF*) model, while sPDC-H more closely aligns with a *nucleation-elongation-secondary nucleation* (*NE2°*) model. Critically, the predictive relationship between $\boldsymbol{\gamma}$ and the assembly mechanisms arises directly from the mass balances constructing the *NEF* and *NE2°* models,[49,54,55] and half time analysis has been previously used to assign *NEF* and *NE2°* models in small molecule supramolecular systems.[52,56] Further considering the models, *NEF* is weakly dependent on concentration, since the mechanism for the formation of nascent fibers (fragmentation) is independent of monomer concentration; Conversely, *NE2°* systems demonstrate strong monomer-dependent rates of assembly, due to the propagation of fibers through the formation of nascent secondary nucleates. These model assignments are necessary for thermodynamic analysis of the underlying self-assembly and gelation processes, and directly point to a material outcome dictated by the different linker chemistries and drug topology of sPDC-E and sPDC-H.

The models were next applied to isothermal gelation curves to extract the relevant rate constants for the *NEF* and *NE2°* processes. Specific rates of interest for these models include those of primary nucleation (k_n), elongation (k_+), fragmentation (k_-), and secondary nucleation (k_2). The corresponding experiments were unseeded, thus yielding coupled rate constants upon solving the material balances in the form of the model corresponding to the specific assembly mechanism. Accordingly, coupled rates in the form of k_nk_+ and k_+k_- were calculated for sPDC-E arising from the *NEF* model while k_nk_+ and k_+k_2 were calculated for sPDC-H arising from the *NE2°* model.

Interestingly, the coupled rate constant involving primary nucleation (k_nk_+) did not show temperature dependent increases in either system, with an overall inverse correlation to temperature (***Fig. S12***). It is theorized that this is due to nucleates which initiate the assembly being less stable at higher temperatures, given the higher kinetic energy of the constituent monomers. Given application of the Arrhenius law is the means of estimating the contributions to the energy barrier of specific assembly processes in these systems, a quantitative analysis of terms involving primary nucleation was not possible. Conversely, the coupled rate constants describing the processes of propagation of the

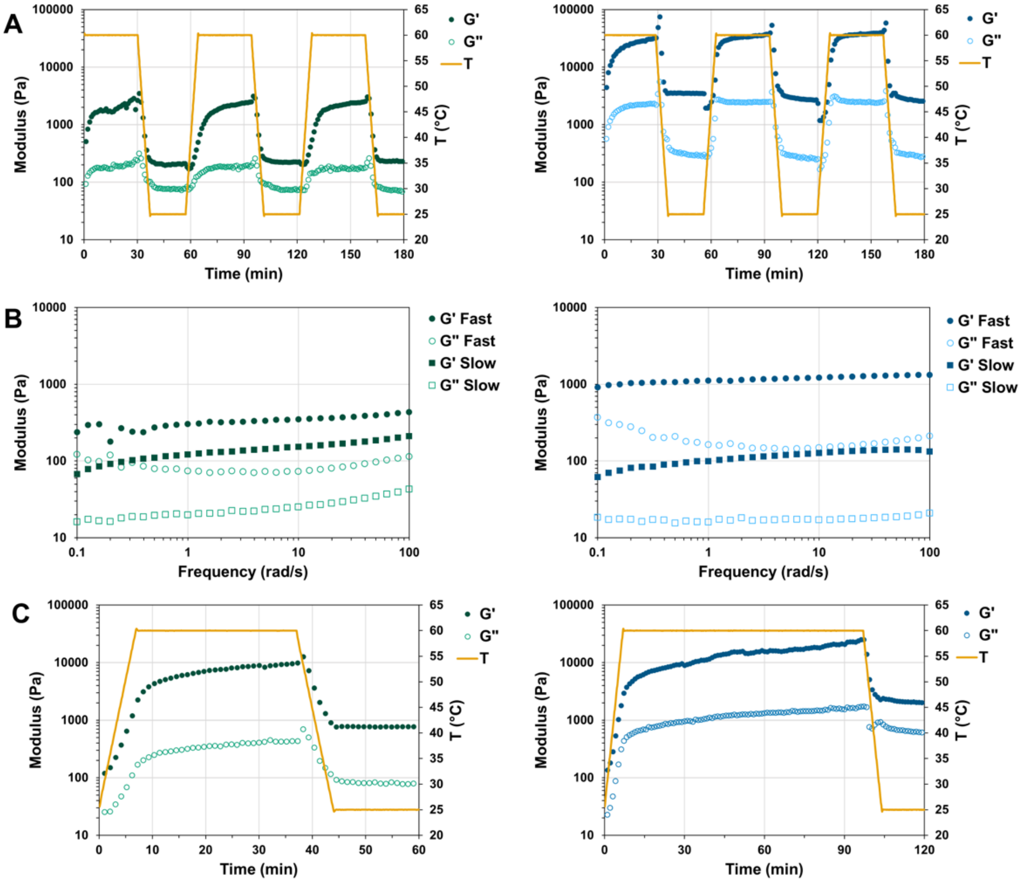

Figure 4: Rheological exploration of thermodynamic states. (**A**) sPDC-E and sPDC-H hydrogels form and adopt higher storage modulus upon heating to 60°C. The gels have reduced storage modulus upon subsequent cooling to 25°C, and cycling demonstrates the two states are reversible. (**B**) Gels produced by the "slow" room temperature path have lower storage modulus than those produced by the "fast" 60°C path. (**C**) Thermal cycling of the "slow" gels again demonstrates the reversibility of thermal equilibria.

fibrous networks ($k_{+}k_{-}$ for sPDC-E, and $k_{+}k_{2}$ for sPDC-H) show strong positive temperature-dependence. Fitting this data to the Arrhenius equation (***Fig. 3C***) allowed the calculation of energy barriers in the propagation processes of sPDC-E (108.5 ± 5.0 kJ/mol) and sPDC-H (226.4 ± 6.6 kJ/mol). This analysis thus provides quantitative evidence that assembly of sPDC-H is more frustrated relative to sPDC-E, aligning with gross observations for more resistant hydrogelation with higher critical concentrations for aggregation and gelation in sPDC-H.

2.3 Rheology: Distinct and Reversible "Hot" and "Cool" Equilibrium Products. A question that arose upon observing thermally induced gelation was whether any structural differences in the materials emerged upon cooling the gels back to ambient temperature, corresponding to changes in the free energy of the systems in each thermal state. Oscillatory rheology offered a means of pursuing this question, and revealed the existence of and reversibility between "hot" (60°C) and "cool" (25°C) equilibrium products for both sPDC-E and sPDC-H. Solutions placed on the rheometer formed gels on initial heating to 60°C, and showed an increase in their energy storage capacity upon equilibration at the "hot" state, with a subsequent reduction in G′ and G′′ upon return to their "cool" thermal state; these states were cyclable at least three times (***Fig. 4A***).

Preliminary observations supported rapid acceleration of gelation upon heating, yet gelation still occurred over longer times at room temperature. As such, it was also interesting to explore the properties of gels developed by this "slow" room temperature path compared to those produced by the "fast" thermally induced path. As shown in ***Fig. 4B***, "slow" gels of both sPDC-E and sPDC-H have relatively lower energy storage capacity in a frequency sweep experiment compared to their "fast" path counterparts. This is likely because the "slow" path allows for sufficient monomer conversion to create an entangled, self-supporting supramolecular network that is above the minimum gelation concentration, but total monomer conversion is incomplete. On thermal cycling, gels initially produced by the "slow" path adopt properties on the same order of magnitude as the "fast" gels, at both the "hot" and "cool" equilibrium states (***Fig. 4A,C***).

2.4 Nanomaterial Implications of Thermodynamic Pathways. Combining results from kinetics and rheology studies of the bulk phase sPDC gels, key thermodynamic products in both systems can be defined: (*i*) spontaneous nucleation, (*ii*) an energetically frustrated route to assembly which can be overcome through heat or over time, and (*iii*) stable, reversible equilibrium products corresponding to a given system temperature. Thus, the next step was to develop further insights into the nanomaterials underlying these gels, and how the prodrug DEX linker chemistry and drug topology were directing these supramolecular outcomes.

Some broad insights in this regard can already be derived from the bulk gel experiments. A notable feature of the sPDC-E and sPDC-H systems is their response to thermal energy. Dehydration of specific domains is key in the formation of β-sheet driven amyloids,[57] and to the self-assembly of thermally gelling polymers.[58] It may be the case that release of waters of hydration contributes to the energy barrier towards β-sheet formation in sPDC-E and sPDC-H. However, dehydration does not appear to be a major energetic barrier in other PA and sPDC systems,[17,19,35] which typically adopt their desired nanomaterial form rapidly at room temperature. Additionally, heat typically shortens fibers in PA networks due to the higher kinetic energy of their constituent β-sheet peptides,[23] so the emergence and persistence of gels driven through β-sheet formation at 60°C is surprising. Indeed, both sPDC-E and sPDC-H gels have their highest storage moduli in the "hot" equilibrium state, implying the strongest β-sheet networks. Importantly, both gels also demonstrated a brief hysteretic effect immediately upon cooling, where the gel modulus briefly increased as temperature decreased (***Fig. 4A,C***). This stiffening period was prolonged when the cooling rate was lowered (***Fig. S13***). This observation is analogous to behavior observed on the annealing of PAs, wherein β-sheet fibers that are weakened upon heating extend and stiffen during cooling.[23] However, this stiffening on initial cooling is not a durable response in sPDC-E and sPDC-H gels, as their moduli eventually trended to a weakened state as temperature was decreased. From this dynamic period, it can be inferred that sPDC-E and sPDC-H β-sheets become temporarily stiffer as the constituent molecules lose kinetic energy on initial cooling, but as they continue to cool other dominant organizing forces of the assembly, very likely including adoption of a preferred orientation in the DEX core, ultimately weaken these β-sheets.

Rheological data also supports a difference in the stiffness, and by extension the relative strengths of β-sheet networks, between the two sPDC systems. The G′ of sPDC-H gels were ~10X higher than those for sPDC-E gels in both the "hot" and "cool" product state (***Fig. 4A***). This is complimentary evidence to the assignment of supramolecular assembly models in the kinetics studies (***Fig. 3C***), as it is reasonable to assume that fibers with stronger β-sheets would be less prone to fragmentation and more likely to propagate through an *NE2°* mechanism. Conversely, the weaker β-sheets of sPDC-E presumably yields flexible fibers that are more prone to fragmentation beyond a critical length.

A final notable feature from rheology is the relative differences in the thermal equilibria of gels produced by the "slow" room temperature path versus the "hot" thermal path (***Fig. 4C***). For sPDC-E gels resulting from thermal cycling, the "slow" products have storage moduli ~8X higher than their "fast" path counterparts, at both the "hot" and "cool" equilibrium. For sPDC-H, the "slow" gel equilibrium moduli are ~2X lower than the "fast" gel. Though rheological properties are an indirect observation of the underlying nanomaterial state, it is clear these differences arise from changes to the physical nature of sPDC nanofibers and their interactions giving rise to network formation. In the case of sPDC-E, it may be that in the low temperature regime, the relative rate of fiber fragmentation is depressed compared to the rate of fiber elongation. When these gels are thermally cycled enabling monomer consumption to reach completion, the result is a network of fewer, but longer, fibers with higher degrees of physical entanglement, leading to a higher storage modulus in the network. Examining sPDC-H, it appears that true thermal equilibrium in the "hot" state is not completely achieved, even after 90 min of incubation. It is thus possible that kinetic-diffusive limitations arise when the assembly reaction is accelerated in a partially complete fiber network, and that an equilibrium product more similar to those of the "fast" path could be achieved given sufficient time.

2.5 Circular Dichroism: Molecular Features of Supramolecular Nanomaterials. To complement studies of the bulk sPDC nanomaterials, circular dichroism (CD) spectroscopy was used to study the supramolecular arrangement of sPDCs. CD was an ideal technique for elucidating changes in the peptide and drug domains of the sPDCs initiated by assembly, as signals of interest were available in the near and far UV range with no overlap. Samples were studied in a similar way to the rheology experiments with instantaneous heating of freshly prepared solutions of monomer equilibrated at 60°C (***Fig. 5A***), followed by instantaneous cooling and equilibration at 25°C (***Fig. 5B***). Concentrations of 0.2% wt. and 0.7% wt. of sPDC-E and sPDC-H, respectively, were above the minimum β-sheet concentration but below the point where sample opacity arising from hydrogelation significantly interfered with data collection (***Fig. S14***).

Dexamethasone disodium phosphate (DEX-P) served as a water-soluble analog to free DEX in control experiments. The intensity of the DEX-P spectra scaled linearly according to concentration (***Fig. S15A***), in

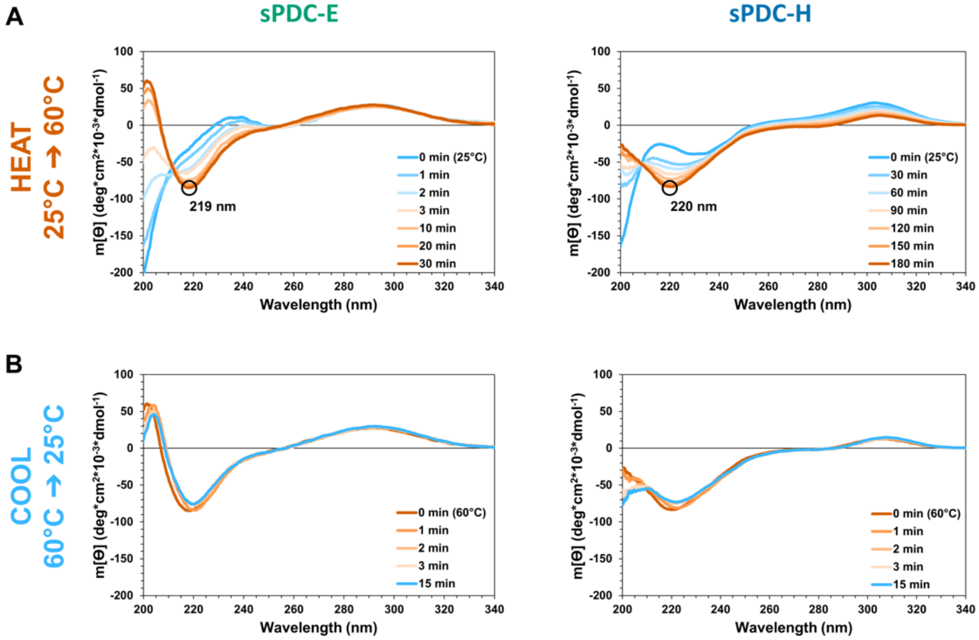

Figure 5: Thermally Cycled CD. (**A**) sPDC-E and sPDC-H CD tracked over time after instantaneous heating from equilibrium at 25°C to 60°C. Minima present at 219 nm (sPDC-E) and 220 nm (sPDC-H) suggest twisted, parallel β-sheet structures. sPDC-H has significant attenuation of the broad DEX signal >300 nm. (**B**) sPDC-E and sPDC-H CD tracked after instantaneous cooling from equilibrium at 60°C to 25°C. Both systems show decreased intensity and bathochromic shifting of the β-sheet minima, indicating weakening and twisting of the β-sheets.

compliance with the Beer-Lambert law, indicating that DEX-P is in a dispersed, non-aggregated state and its spectral bands emerge purely from molecular CD. In particular, the broad positive signal centered at 294 nm was previously noted to be preserved in an ester-linked DEX–peptide conjugate that self-assembled into nanofibrils,[59] and should have no overlap with signals arising from the peptide domain (< 250 nm). In sPDC-E this maximum has a greater signal intensity (28 m[θ]) versus DEX-P (6 m[θ]) (***Fig. 5A left, S15B***), likely due to drug-drug chromophoric interactions and/or solvatohromic effects of DEX being sequestered in the hydrophobic center of assemblies. The intensity and position of the DEX signal changed minimally in the course of thermal cycling (***Fig. 5A left, Fig. 5B, left***). By contrast, the peptide region of the far UV showed a robust transition between secondary structures upon heating, with the disappearance of signal attributable to random coil (minimum <200 nm) and the adoption of β-sheets (maximum: 201 nm, minimum: 219 nm). These are bathochromically shifted relative to the classically reported maxima/minima of 195/216 nm, which is attributed to twisting of the β-sheets.[35] Interestingly, this twisting was accentuated upon cooling to 25°C, with further bathochromic shifting of the β-sheet maximum and minimum (***Fig. 5B, left***). Concomitant with this shifting was a decrease in the intensity of both β-sheet signals, reinforcing the hypothesis developed from rheology of weaker β-sheets in the "cool" thermodynamic product.

Considering sPDC-H, significantly more change was observed in the DEX region of the spectra upon heating. In the initial 25°C trace the broad maximum in the near-UV appears to be preserved (***Fig. 5A, right***), with possible overlap from nascent signals emerging from the chromophore centered on C3 due to modification with the hydrazone bond. Notably, local maxima in the linear UV-absorbance of sPDC-H emerged at 301 and 249 nm, which also complicate the CD spectra (***Fig. S16***). During heating, there is significant attenuation and bathochromic shifting of the broad DEX maxima, indicating changes to the ordering of the drug domains as the nanofibers develop. Additionally, a Cotton effect appears to emerge at ~285 nm as the system equilibrates. While full deconvolution of this signal is difficult due to its likely multichromophoric origin (*syn-* and *anti-* hydrozone-DEX), and overlap with competitive CD signals, on the whole these data suggest a right-handed chiral arrangement of the DEX moieties within the fiber core. The Cotton effect was more obvious in higher concentration samples, but the increased opacity of these makes interpretation of the position difficult (***Fig. S17***). Turning to the peptide domain, sPDC-H revealed a similar evolution as that for sPDC-E, with a twisted β-sheet signal emerging upon heating, and bathochromic shifting and signal reduction upon cooling indicating twisting and weakening of the β-sheets. Also,

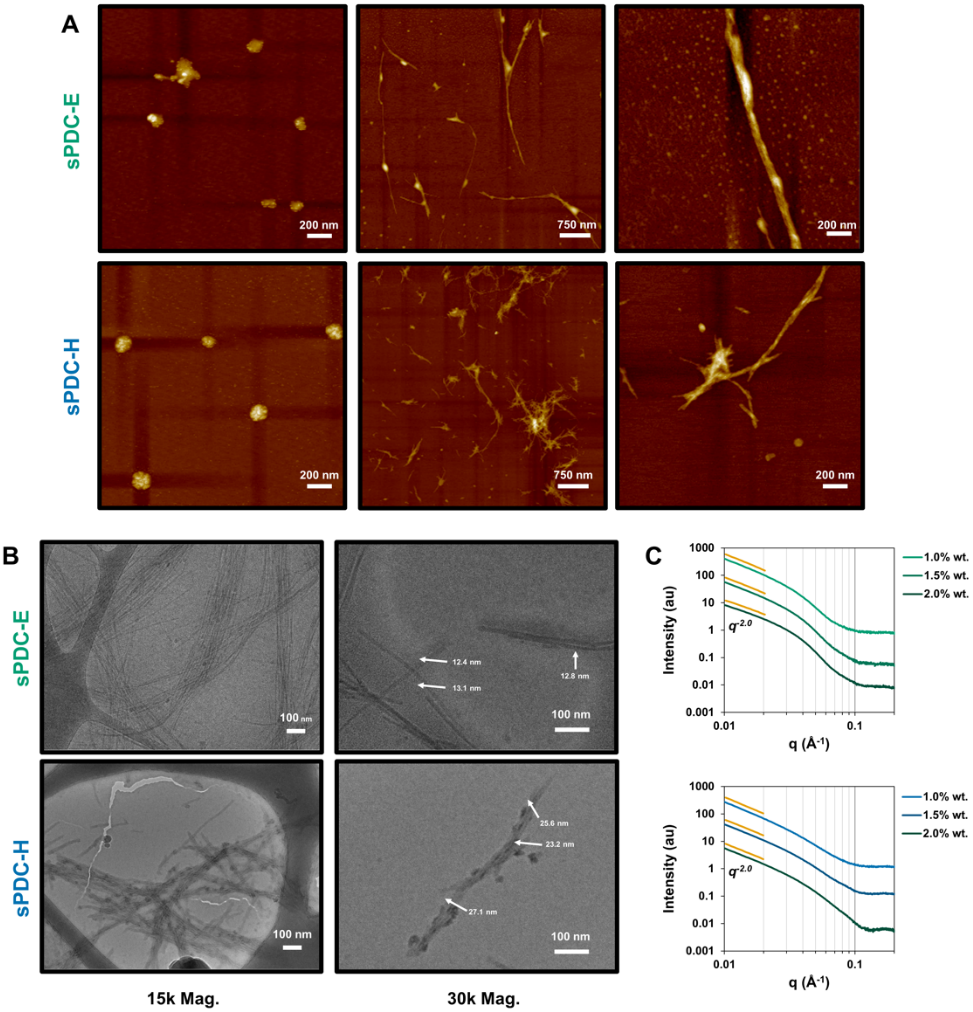

Figure 6: AFM, Cryo-TEM, and SAXS of sPDC nanomaterial states. (**A**) AFM images of freshly dissolved sPDC-E and sPDC-H (*left*), and in the "cool" equilibrium, after the development of fibrils by heating and cooling (*middle,right*). Freshly dissolved sPDCs organize into semi-spherical aggregates, before heating and cooling yields bundled nanofibers. (**B**) Cryo-TEM images of sPDC-E and sPDC-H in their "cool" equilibrium. sPDC-E formed flat, long, and flexible nanostructures with some entanglement. sPDC-H also formed flat nanostructures that were shorter and straighter, with a high degree of inter-fiber twisting. Twisted bundles of sPDC-H fibers were also surface decorated with semi-spherical nodules, suggesting the formation of secondary nucleates in the propagation of nanostructure assembly. (**C**) SAXS spectra of sPDC-E and sPDC-H. Slopes in the low *q* (Guinier) region of q^{-2} indicate the nanostructures have flat/lamellar character.

concentration-dependent sPDC-H experiments reinforced kinetic observations for the strong concentration-dependent assembly mechanism of sPDC-H. While the sPDC-H β-sheet signal takes 3 h to fully emerge and equilibrate at 0.7% wt., this occurs within 30 mins at 1.0% (***Fig. S18***).

2.6 AFM, Cryo-TEM, and SAXS: Inspection of Nanomaterial Form. As a final means of defining the nanomaterial features of the sPDC systems, both atomic force microscopy (AFM) and cryogenic transmission electron microscopy (cryo-TEM) were used to image samples of sPDC-E and sPDC-H at the beginning and end of nanofiber formation. These studies were paired with small angle x-ray scattering (SAXS). In microscopy, concentrations that were identified using CD to be above the critical β-sheet concentration, but below or near the critical gelation concentration, were imaged in order to simplify sample preparation. AFM was conducted on the freshly dissolved materials, (***Fig. 6A, left***) as well as those following heating the sPDCs to 60°C for sufficient time to equilibrate the β-sheets and, cooling to room temperature (***Fig. 6A, middle and right***). This second set of images represent the "cool" equilibrium product, which were also imaged with cryo-TEM (***Fig. 6B***).

Microscopy and X-ray scattering ~~Cryo-TEM and SAXS~~ provided additional morphological details and reinforced understanding of the sPDC-E and sPDC-H nanomaterials derived from kinetics, rheology, and CD experiments. AFM of the freshly dissolved material revealed sPDCs form semi-spherical aggregates of dispersed size. (***Fig. 6A, left***) This suggests a phase separation mechanism may be involved in the initial association of the sPDCs in solution.[60] After thermal cycling, AFM images of "cool" equilibrium products show nanofibrous networks in both materials, with sPDC-E presenting longer, more flexible fibers relative to the shorter twisted formations of sPDC-H. AFM measured z-heights of ~10-15 nm for both materials, and the x-y dimensionality of objects suggests bundling of smaller, individual sPDC nanofibers.

SAXS and cryo-TEM were more suited to capturing the behavior of the sPDC nanofibers in suspension. The slope of SAXS curves in the low *q* (Guinier) region of q^{-2} is indicative of flat/lamellar objects,[61–63] (***Fig. 6C***) which is consistent with the flat and slightly twisted structures observed by Cryo-TEM (***Fig. 6B***). Given this, the sPDC assemblies are best described as ribbon-like nanofibrils. Further comparing the morphologies, sPDC-E presented high aspect-ratio fibrils that were flexible, as evidenced by their smooth and continuous bends, likely due to their weaker β-sheet networks. sPDC-H, conversely, presented shorter, straighter fibrils. Also, the sPDC-H nanofibers were surface-decorated with dark nodules most evident at 30k magnification (***Fig. 6B, bottom right***), providing added evidence for the *NE2°* assembly mechanism initially identified in bulk kinetics studies. Again, these nodules may arise through dehydration of the enriched sPDC liquid phase droplets, in this case catalytically assisted by the sPDC-H fiber surfaces, and serve as the sites of secondary nucleation.[60] The sPDC-H fibrils were about double the width of sPDC-E (***Fig. 6A, right***) and appeared to form tighter bundles, likely contributing to their larger storage modulus in rheology. A last supporting detail from SAXS data was the broad shoulders of the mid-*q* region, most visible in the 2% wt. samples. In sPDC-E the shoulder extended from *q* values corresponding to dimensions of 9-30 nm, while sPDC-H encompassed a slightly larger range from 6-30 nm. This range may capture the average width/height of single fibrils as well as multi-fiber bundles, with the broadness of the signal reflecting significant sample polydispersity.[64]

2.7 Mapping Nanomaterial Forms and Energetic States to a Free Energy Landscape. Combining observations from all studies, a free energy landscape can be described to reflect both the quantitative and qualitative analysis of these sPDC systems in their discrete thermodynamic states (***Fig. 7***). Both sPDCs spontaneously form small-scale metastable nucleates, perhaps even constituting sPDC rich liquid phase droplets in solution,[60] as evidenced by our observation of size disperse spherical aggregates in freshly dissolved sPDC solutions (***Fig. 6A, left***). Once the nucleates form, sPDC-H and sPDC-E confront relatively different energy barriers toward self-assembly to nanofibers, which can be overcome through a "fast" process by thermal energy input, or a "slow" process by sufficient time at room temperature. Once nanostructures form, two thermodynamic minima are apparent corresponding to system temperature. The "hot" (60°C) equilibrium product is characterized by strong β-sheets and some degree of β-sheet twisting. Upon equilibration to the "cool" product, the β-sheets become weaker and their twisting is accentuated (***Fig. 5***). In the absence of heating, the "slow" room temperature product progresses toward this "cool" product over significantly longer times, bypassing the formation of the "hot" conformation that is no longer a stable equilibrium product in a low-temperature regime. It is expected that

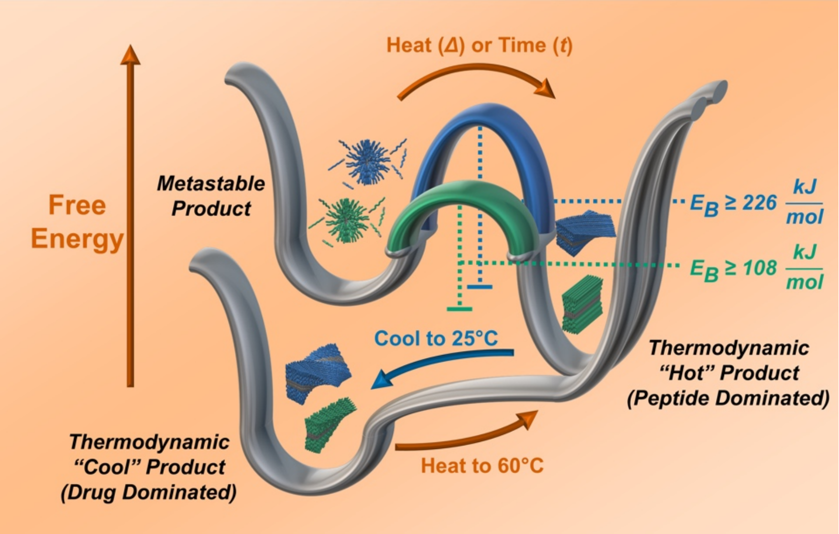

Figure 7: Free Energy Landscape of Divergent Thermodynamic Paths and Discrete Thermodynamic States of sPDC-E and sPDC-H. Both sPDC-E and sPDC-H spontaneously form amphiphilic nucleates ("Metastable Product"). Given time or thermal energy, the nucleates initiate the formation and growth of flat/lamellar nanostructures. The energetic barrier for the kinetic steps governing the growth of the fiber network is roughly double for sPDC-H relative to sPDC-E. Once formed, the sPDC nanostructures can be cycled between discrete thermodynamic states by adjusting the system temperature. At higher temperatures ("Hot" Product), the fiber β-sheets are more rigid and appear the dominant organizing force of the assembly. At lower temperatures ("Cool" Product), the β-sheet structures lose rigidity and increase their degree of twist, yielding to greater drug ordering in the low temperature regime.

in the "cool" equilibrium product, drug–drug interactions have a greater impact on the resulting nanostructure, whereas in the "hot" equilibrium product these interactions yield to greater β-sheet ordering in the peptide domain. In both the "hot" and "cool" equilibrium products, sPDC-H β-sheets were stiffer than those for sPDC-E, as reflected in the 10X larger storage modulus of sPDC-H determined from rheology (***Fig. 4A***). Not reflected in this free energy landscape is the possibility for stable equilibria at intermediate temperatures (*e.g.*, a "warm" product) which would be theoretically attainable by equilibrating at temperatures between 60°C-25°C.

2.8 Analyzing Impacts of Linker Chemistry and Prodrug Topology on sPDC Thermodynamics and Material Forms. Reviewing the molecular structures of these sPDCs and the contributions of the drug domains to the final assembly, an obvious contrast is found in the relative rotational constraints of ester-linked versus hydrazone-linked DEX. While the DEX moiety of sPDC-E has full rotational freedom along the single bonds connecting carbons 17, 20, and 21, as well as the full adipate linker, sPDC-H is not afforded the same flexibility due to the introduction of the hydrazone double bond. sPDC-H is inherently more conformationally limited, an impairment which is likely to frustrate its progress towards stable nucleates capable of initiating nanofiber formation. An additional consideration is the isolated hydrogen bonding functionalities introduced to the hydrophobic core of the assemblies. While sPDC-E carries two hydroxyls, sPDC-H has an additional hydroxyl, plus the hydrazone bond, which has been previously shown as a strong directive cue organizing the hydrophobic core of benzene tricarboximide self-assemblies.[65,66] Both the removal of waters of hydration from the hydrazone, and the necessity of finding hydrogen bonding partners in the core of the assemblies, are enthalpic penalties to the formation of sPDC-H nucleates and nanofibers.

A further consideration is that sPDC-H exists as a racemic mixture of two stereoisomers, likely necessitating a process of self-sorting in order to optimize drug packing, further frustrating the assembly process. While molecular self-sorting is the most thermodynamically favorable arrangement of supramolecular systems of two or more molecules,[67,68] systems are often kinetically trapped in co-assembled energetic minima.[68,69] In practice, self-sorting in multi-component mixtures usually requires the monomers to be sufficiently molecularly distinct,[70,71] or may arise through careful application of kinetic controls.[69] Considering this, it is likely that the sPDC-H nanofibers are a kinetically trapped co-assembly of *syn* and *anti* stereoisomers. While this state is attainable under the kinetic conditions of these experiments, achieving this assembly should be more energetically expensive (time or heat) as compared to thermodynamically idealized self-sorting, or a pure molecular system (sPDC-E).

As sPDC nanofibers form and are cycled between their thermal equilibria, evidence for competitive enthalpic forces in the peptide and drug domains are evident in CD and rheology experiments. In sPDC-H CD, attenuation of the near-UV Dex signal, and the emergence of a positive Cotton effect, are indicators that changes to the initially preferred order of the hydrazone pro-DEX domain are induced by the introduction of ordering to the peptide domain, in the form of β-sheets. Less direct evidence of a similar phenomenon is available in the sPDC-E CD, but this may be due to weaker interactions of the C2-C4 chromophore of the ester-linked DEX. Indeed, turning to the rheological data, both systems show evidence of drug-dominated and peptide-dominated equilibria. While both sPDCs are capable of forming β-sheet supported nanofibers in the "cool" (25°C) thermal state, the rigidity and alignment of these β-sheets increases upon heating, as indicated by the 10X increase in gel stiffness, CD signal intensity growth, and reduction in the degree of β-sheet twisting upon equilibration in the "hot" (60°C) state. Together, these findings suggest that the preferred drug ordering in the "cool" state is frustrating to the formation of more aligned β-sheets, and that the enthalpic energies of drug ordering are dominant in determining the material form on equilibration at lower temperatures. However, upon heating to 60°C, these enthalpic constraints are relieved by the increased kinetic energy of the drug cores, which allows the enthalpic benefits of hydrogen bonding in the peptide β-sheets to dominate the assembly. Again, the transient stiffening of both sPDCs on initial cooling suggests a period where the β-sheets are allowed to further strengthen by annealing, wherein the drug core is still warm enough to allow for rotational and conformational freedom. This is analogous to the annealing behavior seen in traditional PA heating/cooling cycles.[23] Interestingly, sPDC-H presents ~10X greater gel moduli than sPDC-E at both the "hot" and "cool" equilibrium, suggesting that on the whole the ordering imposed by the hydrazone-linked DEX moiety is relatively less hindering to β-sheet formation, notwithstanding other differences in gel network topology.

Though the precise impacts of the molecular structural features on the sPDC assemblies cannot be fully elucidated, the energy barrier of the nanofiber propagation processes in sPDC-H was calculated to be roughly double that of sPDC-E. This suggests the factors of limited rotational freedom, increased hydrogen bonding, and coassembly of stereoisomers are relatively frustrating to the formation of sPDC-H nanofibers compared to the process of sPDC-E assembly. Furthermore, once nanofibers are assembled, both sPDC systems demonstrate significant enthalpic demands in the drug and peptide domain, which in this case are competitive in governing the nano- to macro-scale features of the resulting materials. Clearly, the energetic contributions of drug–drug interactions and linker chemistry to the total assembly are non-zero, and must be considered as an element of rational sPDC nanomaterial preparation. It is projected that this design paradigm will be manifest in sPDC delivery materials having properties such as drug release[15] and bioresponsive function[72] dictated by both their non-covalent interactions and supramolecular landscape of assembly, with these molecular design features being tuned according to need and/or desired application.

3. CONCLUSIONS

Towards the realization and use of sPDCs for advanced drug delivery materials, the contributions of drug supramolecular chemistry to the properties of sPDC assemblies is explored herein. Changing the prodrug chemistry, and by extension the resulting molecular topology, of DEX conjugated to a preserved peptide sequence significantly impacts the assembled nanomaterial properties across length scales. Both sPDC-E and sPDC-H form nanofibrillar structures, but proceed to this state through different mechanisms. Additionally, sPDC-H confronts an energetic barrier to nanofiber propagation about twice that of sPDC-E. Once the nanofibers form, "hot" and "cool" thermal equilibria are attainable which demonstrate competitive enthalpic incentives in the drug and peptide domains of the assemblies, with relative differences between the sPDC-E and sPDC-H being dictated by differential prodrug topology. These findings support the further study of prodrug contributions to sPDC assembly, and demonstrate supramolecular contributions from ordering in the drug domain as an element of rational sPDC design.

4. MATERIALS & METHODS

4.1 Materials. Unless otherwise stated, all materials and reagents were purchased from commercial vendors and used as received. Solid phase peptide synthesis reagents, including Fluorenylmethyloxycarbonyl protected amino acids, Rink Amide AM Resin, Oxyma, Diisoproylcarbodimide, hexafluorophosphate benzotriazole tetramethyl uronium, N,N-Diisopropylethylamine, hexafluoroisopropanol, and Trifluoroacetic Acid were purchased from ChemImpex International Inc. All other chemicals referenced were purchased from commercial vendors through VWR International.

4.2 Synthesis. Detailed synthetic methods for the hydrazide linker, sPDC-H, and sPDC-E are provided in the Online Supporting Information. The syntheses are summarized in ***Schemes S1-S3*** and ^{1}H NMR spectra of key intermediates and the product of the hydrazide linker synthesis are given in ***Figs. S1-S4.*** ESI-MS spectra and analytical-HPLC traces for sPDC-H and sPDC-E are given in ***Fig. S5-S6.*** Synthetic strategies for the hydrazide linker were adapted from reported methods.[73] Synthetic strategies for sPDC-E synthesis were also adapted from reported methods.[37]

4.3 Thermally Induced Hydrogelation Kinetics. sPDC-E and sPDC-H samples were dissolved in 400 μL of DI water, and diluted with and equal volume of 120 mM phosphate buffer (pH 7.2) to achieve a final volume of 800 μL, the desired sPDC concentration, and phosphate concentration of 60 mM. Samples were transferred to disposable polystyrene cuvettes and a thin layer of mineral oil was pipetted above the aqueous sample to prevent evaporation into the headspace of the cuvette during experiments. Based upon observation during the initial hydrogelation surveys at 60°C, isothermal gelation curves were monitored at temperatures between 55°C-65°C, yielding kinetic results with reasonable experiment times of 45 minutes. Percent transmittance at 600 nm was recorded (*Thermo Scientific Evolution 201 UV-Vis Spectrophotometer*) with Peltier temperature control. Data were normalized, uploaded to the web based *Amylofit* data analysis program (https://amylofit.com), and processed using online instructions and the published *Amylofit* protocol.[53] Models were fit to the individual curves of the isothermal experiments, and reaction orders of primary and secondary nucleation were held at 2 as global fixed parameters.

4.4 Rheology. For thermally gelled samples, solutions of sPDC-E and sPDC-H were dissolved in DI water at 4% w/v and diluted with an equal volume of 100 mM phosphate buffer (pH 7.2) to achieve a final concentration of 2% w/v sPDC and 50 mM phosphate at pH 7.4. Samples were immediately pipetted to the lower geometry of the rheometer (*TA Instruments HR-2 Discovery Hybrid Rheometer*). The upper geometry was a 25 mm parallel stainless steel plate, and the geometry gap was set to 200 μm. The upper and lower geometries were sealed with a thin layer of silicon oil to prevent drying of the sample. Oscillatory rheology data was collected as samples were heated, cooled, and incubated at various thermal states. For samples gelled at room temperature, sPDC solutions were prepared in the same way and stored at room temperature for 7 d. The gels were pipetted to the rheometer lower geometry and studied in the same way as the thermally induced gels.

4.5 Circular Dichroism. CD samples were dissolved in DI water at 0.4% w/v and 1.4% w/v for sPDC-E and sPDC-H, respectively. The samples were diluted with an equal volume of 100 mM phosphate buffer (pH 7.2). 45 μL of sPDC solution was pipetted to the well of a 0.1 mm pathlength O-shaped demountable CD cuvette (*Firefly Scientific*) and the cuvette was carefully sealed. CD spectra were collected (*Jasco J-1700 CD Spectrometer equipped with a Koolance Exos Liquid Cooling System*) in 65 s scans on freshly dissolved samples and those incubated in various thermal states.

4.6 Small-Angle X-ray Scattering. The sPDC samples were dissolved in DI and diluted with an equal volume of 100 mM phosphate buffer (pH 7.2) to achieve the desired sPDC concentration. The solutions were pipetted to 1.5 mm quartz capillaries which were sealed with wax, and the sPDCs were gelled by incubation in a 60°C water bath for 1 h. SAXS spectra were collected at the Advanced Photon Source synchrotron beamline 12-ID-B, operated by the Chemical and Materials Science group at Argonne National Laboratory. Beam parameters were as follows: X-ray beam wavelength = 0.9322 Å (energy of 13.3 keV); exposure time = 0.1 s.

4.7 Atomic Force Microscopy. To image freshly dissolved sPDCs, samples were dissolved in DI water at 0.4% w/v and 1.4% w/v for sPDC-E and sPDC-H, respectively, and diluted with an equal volume of 100 mM phosphate buffer (pH 7.2). For assembled samples, the sPDCs were dissolved in the same way and solutions were incubated in a 60°C water bath for 1 h and 3 h for sPDC-E and sPDC-H, respectively. Twenty µL of each solution was deposited on a mica surface, set for 30 s, and absorbed by filter paper. The mica samples were further dried by a stream of nitrogen and under vacuum overnight. AFM images (*Park XE7*) were acquired in non-contact mode using a non-contact cantilever (PPP-NCHR, Park Systems; tip radius < 10 nm, force constant = 42 N/m, resonance frequency = 330 kHz).

4.8 Cryogenic Transmission Electron Microscopy. sPDC samples were dissolved in DI water at 0.4% w/v and 1.4% w/v for sPDC-E and sPDC-H, respectively, and diluted with an equal volume of 100 mM phosphate buffer (pH 7.2). The solutions were incubated in a 60°C water bath for 1 h and 3 h for sPDC-E and sPDC-H, respectively. Cryo-TEM samples were prepared by incubating 5 µL of sPDC solutions on lacey carbon/formvar grids (*Ted Pella*) for 60 s, followed by 2×5 s on each side using a Leica EM GP2 automatic plunge freezer. Visualization of the prepared cryo-TEM samples performed (*JEOL 2011 TEM*) at an accelerating voltage of 120 kV.

ASSOCIATED CONTENT

Supporting Information

The Supporting Information is available free of charge on the ACS Publications website:

> Detailed synthetic methods and schematics for the hydrazide linker species, sPDC-H, and sPDC-E. Molecular characterization of hydrazide linker intermediates, sPDC-H, and sPDC-E. Bulk release assay, nile red critical aggregation concentration assay, and additional gelation kinetics, rheology, and CD experiments. (.PDF)

AUTHOR INFORMATION

Corresponding Author

* mwebber@nd.edu

Notes

The authors declare no competing financial interests.

ACKNOWLEDGMENT

MJW gratefully acknowledges funding support for this work from the National Science Foundation (BMAT, 1944875), the National Institutes of Health (R35GM137987), a 3M Non-Tenured Faculty Award (3M Company), and the University of Notre Dame Berthiaume Institute for Precision Health (2019 Discovery Award). This research used resources of the Advanced Photon Source, a U.S. Department of Energy (DOE) Office of Science User Facility operated for the DOE Office of Science by Argonne National Laboratory under Contract No. DE-AC02-06CH11357. We are grateful for the support of Prof. Jennifer Schaefer (Notre Dame) and her laboratory in facilitating SAXS studies. Cryo-TEM imaging was carried out in the Notre Dame Integrated Imaging Facility using the JEOL 2011 TEM. We thank Maksym Zhukovskyi, Ph.D., for knowledge, expertise, and time towards this research. We also thank the ND Energy Materials Characterization Facility for use of the TA Instruments HR-2 Discovery Hybrid Rheometer and Park XE7 AFM, Prof. Yichun Wang's Lab (Notre Dame) for use of their CD Spectrometer, and the Prof. Bradley Smith's Lab (Notre Dame) for use of their Spectrofluorometer.

REFERENCES

(1) Kakkar, A.; Traverso, G.; Farokhzad, O. C.; Weissleder, R.; Langer, R. Evolution of Macromolecular Complexity in Drug Delivery Systems. *Nat Rev Chem* **2017**, *1* (8). https://doi.org/10.1038/s41570-017-0063.

(2) Webber, M. J.; Langer, R. Drug Delivery by Supramolecular Design. *Chem. Soc. Rev.* **2017**, *46* (21), 6600–6620.

(3) Wang, F.; Xu, D.; Su, H.; Zhang, W.; Sun, X.; Monroe, M. K.; Chakroun, R. W.; Wang, Z.; Dai, W.; Oh, R.; Wang, H.; Fan, Q.; Wan, F.; Cui, H. Supramolecular Prodrug Hydrogelator as an Immune Booster for Checkpoint Blocker–based Immunotherapy. *Science Advances*. 2020, p eaaz8985. https://doi.org/10.1126/sciadv.aaz8985.

(4) Wang, F.; Su, H.; Lin, R.; Chakroun, R. W.; Monroe, M. K.; Wang, Z.; Porter, M.; Cui, H. Supramolecular Tubustecan Hydrogel as Chemotherapeutic Carrier to Improve Tumor Penetration and Local Treatment Efficacy. *ACS Nano* **2020**, *14* (8), 10083–10094.

(5) Ji, Y.; Xiao, Y.; Xu, L.; He, J.; Qian, C.; Li, W.; Wu, L.;

Chen, R.; Wang, J.; Hu, R.; Zhang, X.; Gu, Z.; Chen, Z. Drug-Bearing Supramolecular MMP Inhibitor Nanofibers for Inhibition of Metastasis and Growth of Liver Cancer. *Adv. Sci.* **2018**, *5* (8), 1700867.

(6) Cui, H.; Cheetham, A. G.; Pashuck, E. T.; Stupp, S. I. Amino Acid Sequence in Constitutionally Isomeric Tetrapeptide Amphiphiles Dictates Architecture of One-Dimensional Nanostructures. *J. Am. Chem. Soc.* **2014**, *136* (35), 12461–12468.

(7) Choi, S.-J.; Kwon, S. H.; Lim, Y.-B. 3D2 Self-Assembling Janus Peptide Dendrimers with Tailorable Supermultivalency. *Advanced Functional Materials*. 2019, p 1808020. https://doi.org/10.1002/adfm.201808020.

(8) Webber, M. J. Engineering Responsive Supramolecular Biomaterials: Toward Smart Therapeutics. *Bioeng Transl Med* **2016**, *1* (3), 252–266.

(9) Wu, H.; Zhong, D.; Zhang, Z.; Li, Y.; Zhang, X.; Li, Y.; Zhang, Z.; Xu, X.; Yang, J.; Gu, Z. Bioinspired Artificial Tobacco Mosaic Virus with Combined Oncolytic Properties to Completely Destroy Multidrug-Resistant Cancer. *Advanced Materials*. 2020, p 2005181. https://doi.org/10.1002/adma.202005181.

(10) Son, J.; Kalafatovic, D.; Kumar, M.; Yoo, B.; Cornejo, M. A.; Contel, M.; Ulijn, R. V. Customizing Morphology, Size, and Response Kinetics of Matrix Metalloproteinase-Responsive Nanostructures by Systematic Peptide Design. *ACS Nano* **2019**, *13* (2), 1555–1562.

(11) Wang, Y.; Cheetham, A. G.; Angacian, G.; Su, H.; Xie, L.; Cui, H. Peptide–drug Conjugates as Effective Prodrug Strategies for Targeted Delivery. *Advanced Drug Delivery Reviews*. 2017, pp 112–126. https://doi.org/10.1016/j.addr.2016.06.015.

(12) Sis, M. J.; Webber, M. J. Drug Delivery with Designed Peptide Assemblies. *Trends Pharmacol. Sci.* **2019**, *40* (10), 747–762.

(13) Su, H.; Koo, J. M.; Cui, H. One-Component Nanomedicine. *J. Control. Release* **2015**, *219*, 383–395.

(14) Lin, R.; Cheetham, A. G.; Zhang, P.; Lin, Y.-A.; Cui, H. Supramolecular Filaments Containing a Fixed 41% Paclitaxel Loading. *Chem. Commun.* **2013**, *49* (43), 4968–4970.

(15) Chakroun, R. W.; Wang, F.; Lin, R.; Wang, Y.; Su, H.; Pompa, D.; Cui, H. Fine-Tuning the Linear Release Rate of Paclitaxel-Bearing Supramolecular Filament Hydrogels through Molecular Engineering. *ACS Nano* **2019**, *13* (7), 7780–7790.

(16) Wang, Y.; Kaur, K.; Scannelli, S. J.; Bitton, R.; Matson, J. B. Self-Assembled Nanostructures Regulate HS Release from Constitutionally Isomeric Peptides. *J. Am. Chem. Soc.* **2018**, *140* (44), 14945–14951.

(17) Cheetham, A. G.; Zhang, P.; Lin, Y.-A.; Lin, R.; Cui, H. Synthesis and Self-Assembly of a Mikto-Arm Star Dual Drug Amphiphile Containing Both Paclitaxel and Camptothecin. *J. Mater. Chem. B Mater. Biol. Med.* **2014**, *2* (42), 7316–7326.

(18) Wang, F.; Su, H.; Xu, D.; Dai, W.; Zhang, W.; Wang, Z.; Anderson, C. F.; Zheng, M.; Oh, R.; Wan, F.; Cui, H. Tumour Sensitization via the Extended Intratumoural Release of a STING Agonist and Camptothecin from a Self-Assembled Hydrogel. *Nat Biomed Eng* **2020**, *4* (11), 1090–1101.

(19) Chen, Z.; Xing, L.; Fan, Q.; Cheetham, A. G.; Lin, R.; Holt, B.; Chen, L.; Xiao, Y.; Cui, H. Drug-Bearing Supramolecular Filament Hydrogels as Anti-Inflammatory Agents. *Theranostics* **2017**, *7* (7), 2003–2014.

(20) Wang, F.; Su, H.; Xu, D.; Monroe, M. K.; Anderson, C. F.; Zhang, W.; Oh, R.; Wang, Z.; Sun, X.; Wang, H.; Wan, F.; Cui, H. Therapeutic Supramolecular Tubustecan Hydrogel Combined with Checkpoint Inhibitor Elicits Immunity to Combat Cancer. *Biomaterials* **2021**, *279*, 121182.

(21) Wang, J.; Hu, S.; Mao, W.; Xiang, J.; Zhou, Z.; Liu, X.; Tang, J.; Shen, Y. Assemblies of Peptide-Cytotoxin Conjugates for Tumor-Homing Chemotherapy. *Advanced Functional Materials*. 2019, p 1904925. https://doi.org/10.1002/adfm.201904925.

(22) Sorrenti, A.; Leira-Iglesias, J.; Markvoort, A. J.; de Greef, T. F. A.; Hermans, T. M. Non-Equilibrium Supramolecular Polymerization. *Chem. Soc. Rev.* **2017**, *46* (18), 5476–5490.

(23) Tantakitti, F.; Boekhoven, J.; Wang, X.; Kazantsev, R. V.; Yu, T.; Li, J.; Zhuang, E.; Zandi, R.; Ortony, J. H.; Newcomb, C. J.; Palmer, L. C.; Shekhawat, G. S.; de la Cruz, M. O.; Schatz, G. C.; Stupp, S. I. Energy Landscapes and Functions of Supramolecular Systems. *Nat. Mater.* **2016**, *15* (4), 469–476.

(24) Yu, S.; Xian, S.; Ye, Z.; Pramudya, I.; Webber, M. J. Glucose-Fueled Peptide Assembly: Glucagon Delivery via Enzymatic Actuation. *J. Am. Chem. Soc.* **2021**, *143* (32), 12578–12589.

(25) Kang, M.; Zhang, P.; Cui, H.; Loverde, S. M. - Stacking Mediated Chirality in Functional Supramolecular Filaments. *Macromolecules* **2016**, *49* (3), 994–1001.

(26) Kang, M.; Cui, H.; Loverde, S. M. Coarse-Grained Molecular Dynamics Studies of the Structure and Stability of Peptide-Based Drug Amphiphile Filaments. *Soft Matter* **2017**, *13* (42), 7721–7730.

(27) Manandhar, A.; Chakraborty, K.; Tang, P. K.; Kang, M.; Zhang, P.; Cui, H.; Loverde, S. M. Rational Coarse-Grained Molecular Dynamics Simulations of Supramolecular Anticancer Nanotubes. *J. Phys. Chem. B* **2019**, *123* (50), 10582–10593.

(28) Wang, J.; Hu, S.; Mao, W.; Xiang, J.; Zhou, Z.; Liu, X.; Tang, J.; Shen, Y. Assemblies of Peptide-Cytotoxin Conjugates for Tumor-Homing Chemotherapy. *Advanced Functional Materials*. 2019, p 1807446. https://doi.org/10.1002/adfm.201807446.

(29) National Center for Biotechnology Information. PubChem Compound Summary for CID 5743, Dexamethasone. https://pubchem.ncbi.nlm.nih.gov/compound/Dexamethasone. Accessed Nov. 2, 2021 https://pubchem.ncbi.nlm.nih.gov/compound/5743 (accessed 2021 -11 -02).

(30) Liu, Q.; Zhan, C.; Barhoumi, A.; Wang, W.; Santamaria, C.; McAlvin, J. B.; Kohane, D. S. A Supramolecular Shear-Thinning Anti-Inflammatory Steroid Hydrogel. *Advanced Materials*. 2016, pp 6680–6686. https://doi.org/10.1002/adma.201601147.

(31) Zhang, Z.; Yu, J.; Zhou, Y.; Zhang, R.; Song, Q.; Lei, L.; Li, X. Supramolecular Nanofibers of Dexamethasone Derivatives to Form Hydrogel for Topical Ocular Drug Delivery. *Colloids Surf. B Biointerfaces* **2018**, *164*, 436–443.

(32) Cui, H.; Webber, M. J.; Stupp, S. I. Self-Assembly of Peptide Amphiphiles: From Molecules to Nanostructures to Biomaterials. *Biopolymers* **2010**, *94* (1), 1–18.

(33) Levitt, M. Conformational Preferences of Amino Acids in Globular Proteins. *Biochemistry* **1978**, *17* (20), 4277–4285.

(34) Kim, C. A.; Berg, J. M. Thermodynamic β -Sheet Propensities Measured Using a Zinc-Finger Host Peptide. *Nature*. 1993, pp 267–270. https://doi.org/10.1038/362267a0.

(35) Pashuck, E. T.; Cui, H.; Stupp, S. I. Tuning Supramolecular Rigidity of Peptide Fibers through Molecular Structure. *J. Am. Chem. Soc.* **2010**, *132* (17), 6041–6046.

(36) Ortony, J. H.; Newcomb, C. J.; Matson, J. B.; Palmer, L. C.; Doan, P. E.; Hoffman, B. M.; Stupp, S. I. Internal Dynamics of a Supramolecular Nanofibre. *Nat. Mater.* **2014**, *13* (8), 812–816.

(37) Formica, F. A.; Barreto, G.; Zenobi-Wong, M. Cartilage-Targeting Dexamethasone Prodrugs Increase the Efficacy of Dexamethasone. *J. Control. Release* **2019**, *295*, 118–129.

(38) Webber, M. J.; Matson, J. B.; Tamboli, V. K.; Stupp, S. I. Controlled Release of Dexamethasone from Peptide Nanofiber Gels to Modulate Inflammatory Response. *Biomaterials* **2012**, *33* (28), 6823–6832.

(39) Liu, X.-M.; Quan, L.-D.; Tian, J.; Laquer, F. C.; Ciborowski, P.; Wang, D. Syntheses of Click PEG-Dexamethasone Conjugates for the Treatment of Rheumatoid Arthritis. *Biomacromolecules* **2010**, *11* (10), 2621–2628.

(40) Quan, L.-D.; Yuan, F.; Liu, X.-M.; Huang, J.-G.; Alnouti, Y.; Wang, D. Pharmacokinetic and Biodistribution Studies of N-(2-Hydroxypropyl)methacrylamide Copolymer-Dexamethasone Conjugates in Adjuvant-Induced Arthritis Rat Model. *Molecular Pharmaceutics*. 2010, pp 1041–1049. https://doi.org/10.1021/mp100132h.

(41) Li, C.; Li, H.; Wang, Q.; Zhou, M.; Li, M.; Gong, T.; Zhang, Z.; Sun, X. pH-Sensitive Polymeric Micelles for Targeted Delivery to Inflamed Joints. *J. Control. Release* **2017**, *246*, 133–141.

(42) Wang, D.; Miller, S. C.; Liu, X.-M.; Anderson, B.; Wang, X. S.; Goldring, S. R. Novel Dexamethasone-HPMA Copolymer Conjugate and Its Potential Application in Treatment of Rheumatoid Arthritis. *Arthritis Res. Ther.* **2007**, *9* (1), R2.

(43) Jia, Z.; Wang, X.; Wei, X.; Zhao, G.; Foster, K. W.; Qiu, F.; Gao, Y.; Yuan, F.; Yu, F.; Thiele, G. M.; Bronich, T. K.; O'Dell, J. R.; Wang, D. Micelle-Forming Dexamethasone Prodrug Attenuates Nephritis in Lupus-Prone Mice without Apparent Glucocorticoid Side Effects. *ACS Nano* **2018**, *12* (8), 7663–7681.

(44) Bajpayee, A. G.; Quadir, M. A.; Hammond, P. T.; Grodzinsky, A. J. Charge Based Intra-Cartilage Delivery of Single Dose Dexamethasone Using Avidin Nano-Carriers Suppresses Cytokine-Induced Catabolism Long Term. *Osteoarthritis Cartilage* **2016**, *24* (1), 71–81.

(45) Dexamethasone Conjugation to Biodegradable Avidin-Nucleic-Acid-Nano-Assemblies Promotes Selective Liver Targeting and Improves Therapeutic Efficacy in an Autoimmune Hepatitis Murine Model. https://doi.org/10.1021/acsnano.8b09655.s001.

(46) Jia, Z.; Zhao, G.; Wei, X.; Kong, D.; Sun, Y.; Zhou, Y.; Lele, S. M.; Fehringer, E. V.; Garvin, K. L.; Goldring, S. R.; Wang, D. Structural Optimization of HPMA Copolymer-Based Dexamethasone Prodrug for Improved Treatment of Inflammatory Arthritis. *J. Control. Release* **2020**, *324*, 560–573.

(47) Preslar, A. T.; Parigi, G.; McClendon, M. T.; Sefick, S. S.; Moyer, T. J.; Haney, C. R.; Waters, E. A.; MacRenaris, K. W.; Luchinat, C.; Stupp, S. I.; Meade, T. J. Gd(III)-Labeled Peptide Nanofibers for Reporting on Biomaterial Localization in Vivo. *ACS Nano* **2014**, *8* (7), 7325–7332.

(48) Li, Q.; Zhang, G.; Wu, Y.; Wang, Y.; Liang, Y.; Yang, X.; Qi, W.; Su, R.; He, Z. Control of Peptide Hydrogel Formation and Stability via Heating Treatment. *J. Colloid Interface Sci.* **2021**, *583*, 234–242.

(49) Knowles, T. P. J.; Waudby, C. A.; Devlin, G. L.; Cohen, S. I. A.; Aguzzi, A.; Vendruscolo, M.; Terentjev, E. M.; Welland, M. E.; Dobson, C. M. An Analytical Solution to the Kinetics of Breakable Filament Assembly. *Science* **2009**, *326* (5959), 1533–1537.

(50) Zimmermann, M. R.; Bera, S. C.; Meisl, G.; Dasadhikari, S.; Ghosh, S.; Linse, S.; Garai, K.; Knowles, T. P. J. Mechanism of Secondary Nucleation at the Single Fibril Level from Direct Observations of Aβ42 Aggregation. *Journal of the American Chemical Society*. 2021, pp 16621–16629. https://doi.org/10.1021/jacs.1c07228.

(51) Spitzer, D.; Marichez, V.; Formon, G. J. M.; Besenius, P.; Hermans, T. M. Surface-Assisted Self-Assembly of a Hydrogel by Proton Diffusion. *Angew. Chem. Int. Ed Engl.* **2018**, *57* (35), 11349–11353.

(52) Singh, N.; Lainer, B.; Formon, G. J. M.; De Piccoli, S.; Hermans, T. M. Re-Programming Hydrogel Properties Using a Fuel-Driven Reaction Cycle. *J. Am. Chem. Soc.* **2020**, *142* (9), 4083–4087.

(53) Meisl, G.; Kirkegaard, J. B.; Arosio, P.; Michaels, T. C. T.; Vendruscolo, M.; Dobson, C. M.; Linse, S.; Knowles, T. P. J. Molecular Mechanisms of Protein Aggregation from Global Fitting of Kinetic Models. *Nat. Protoc.* **2016**, *11* (2), 252–272.

(54) Cohen, S. I. A.; Linse, S.; Luheshi, L. M.; Hellstrand, E.; White, D. A.; Rajah, L.; Otzen, D. E.; Vendruscolo, M.; Dobson, C. M.; Knowles, T. P. J. Proliferation of Amyloid-β42 Aggregates Occurs through a Secondary

Nucleation Mechanism. *Proc. Natl. Acad. Sci. U. S. A.* **2013**, *110* (24), 9758–9763.

(55) Michaels, T. C. T.; Cohen, S. I. A.; Vendruscolo, M.; Dobson, C. M.; Knowles, T. P. J. Hamiltonian Dynamics of Protein Filament Formation. *Phys. Rev. Lett.* **2016**, *116* (3), 038101.

(56) Leira-Iglesias, J.; Tassoni, A.; Adachi, T.; Stich, M.; Hermans, T. M. Oscillations, Travelling Fronts and Patterns in a Supramolecular System. *Nature Nanotechnology*. 2018, pp 1021–1027. https://doi.org/10.1038/s41565-018-0270-4.

(57) Balbirnie, M.; Grothe, R.; Eisenberg, D. S. An Amyloid-Forming Peptide from the Yeast Prion Sup35 Reveals a Dehydrated Beta-Sheet Structure for Amyloid. *Proc. Natl. Acad. Sci. U. S. A.* **2001**, *98* (5), 2375–2380.

(58) Dou, Q. Q.; Liow, S. S.; Ye, E.; Lakshminarayanan, R.; Loh, X. J. Biodegradable Thermogelling Polymers: Working towards Clinical Applications. *Adv. Healthc. Mater.* **2014**, *3* (7), 977–988.

(59) Tang, W.; Zhao, Z.; Chong, Y.; Wu, C.; Liu, Q.; Yang, J.; Zhou, R.; Lian, Z.-X.; Liang, G. Tandem Enzymatic Self-Assembly and Slow Release of Dexamethasone Enhances Its Antihepatic Fibrosis Effect. *ACS Nano* **2018**, *12* (10), 9966–9973.

(60) Yuan, C.; Levin, A.; Chen, W.; Xing, R.; Zou, Q.; Herling, T. W.; Challa, P. K.; Knowles, T. P. J.; Yan, X. Nucleation and Growth of Amino Acid and Peptide Supramolecular Polymers through Liquid–Liquid Phase Separation. *Angewandte Chemie*. 2019, pp 18284–18291. https://doi.org/10.1002/ange.201911782.

(61) Cui, H.; Muraoka, T.; Cheetham, A. G.; Stupp, S. I. Self-Assembly of Giant Peptide Nanobelts. *Nano Lett.* **2009**, *9* (3), 945–951.

(62) Sahoo, J. K.; VandenBerg, M. A.; Ruiz Bello, E. E.; Nazareth, C. D.; Webber, M. J. Electrostatic-Driven Self-Sorting and Nanostructure Speciation in Self-Assembling Tetrapeptides. *Nanoscale* **2019**, *11* (35), 16534–16543.

(63) Moyer, T. J.; Cui, H.; Stupp, S. I. Tuning Nanostructure Dimensions with Supramolecular Twisting. *J. Phys. Chem. B* **2013**, *117* (16), 4604–4610.

(64) VandenBerg, M. A.; Sahoo, J. K.; Zou, L.; McCarthy, W.; Webber, M. J. Divergent Self-Assembly Pathways to Hierarchically Organized Networks of Isopeptide-Modified Discotics under Kinetic Control. *ACS Nano* **2020**, *14* (5), 5491–5505.

(65) Trausel, F.; Versluis, F.; Maity, C.; Poolman, J. M.; Lovrak, M.; van Esch, J. H.; Eelkema, R. Catalysis of Supramolecular Hydrogelation. *Acc. Chem. Res.* **2016**, *49* (7), 1440–1447.

(66) Boekhoven, J.; Poolman, J. M.; Maity, C.; Li, F.; van der Mee, L.; Minkenberg, C. B.; Mendes, E.; van Esch, J. H.; Eelkema, R. Catalytic Control over Supramolecular Gel Formation. *Nat. Chem.* **2013**, *5* (5), 433–437.

(67) Wu, A.; Isaacs, L. Self-Sorting: The Exception or the Rule? *Journal of the American Chemical Society*. 2003, pp 4831–4835. https://doi.org/10.1021/ja028913b.

(68) Görl, D.; Zhang, X.; Stepanenko, V.; Würthner, F. Supramolecular Block Copolymers by Kinetically Controlled Co-Self-Assembly of Planar and Core-Twisted Perylene Bisimides. *Nat. Commun.* **2015**, *6*, 7009.

(69) Morris, K. L.; Chen, L.; Raeburn, J.; Sellick, O. R.; Cotanda, P.; Paul, A.; Griffiths, P. C.; King, S. M.; O'Reilly, R. K.; Serpell, L. C.; Adams, D. J. Chemically Programmed Self-Sorting of Gelator Networks. *Nat. Commun.* **2013**, *4*, 1480.

(70) Draper, E. R.; Eden, E. G. B.; McDonald, T. O.; Adams, D. J. Spatially Resolved Multicomponent Gels. *Nat. Chem.* **2015**, *7* (10), 848–852.

(71) Onogi, S.; Shigemitsu, H.; Yoshii, T.; Tanida, T.; Ikeda, M.; Kubota, R.; Hamachi, I. In Situ Real-Time Imaging of Self-Sorted Supramolecular Nanofibres. *Nat. Chem.* **2016**, *8* (8), 743–752.

(72) Gong, Z.; Shi, Y.; Tan, H.; Wang, L.; Gao, Z.; Lian, B.; Wang, G.; Sun, H.; Sun, P.; Zhou, B.; Bai, J. Plasma Amine Oxidase-Induced Nanoparticle-to-Nanofiber Geometric Transformation of an Amphiphilic Peptide for Drug Encapsulation and Enhanced Bactericidal Activity. *ACS Appl. Mater. Interfaces* **2020**, *12* (4), 4323–4332.

(73) Matson, J. B.; Stupp, S. I. Drug Release from Hydrazone-Containing Peptide Amphiphiles. *Chem. Commun.* **2011**, *47* (28), 7962–7964.